# Optoelectrode based on conductive fiber Fabry-Perot probe for simultaneous electrochemical and optical sensing

Xinyu Chang[a], Xingyue Wen[a], Danheng Gao[a], Meng Luo[a], Pingping Teng[a], Zheng Zhu[a,*], Jianzhong Zhang[a], Kang Li[b], Nigel Copner[b], Xinghua Yang[a,*]

[a]Key Laboratory of In-Fiber Integrated Optics, Ministry of Education, College of Physics and Optoelectronic Engineering, Harbin Engineering University, Harbin 150001, China

[b]Wireless & Optoelectronics Research & Innovation Centre, Faculty of Computing, Engineering & Science, University of South Wales, Wales, CF37 1DL, UK

Fax: 0086-451-82519850

Phone: 0086-451-82519850

E-mail:*yangxh@hrbeu.edu.cn; zhuzheng@hrbeu.edu.cn

Keywords: Optoelectrode; Fiber Fabry–Perot cavity probe; Indium tin oxide; Optical fiber sensor

## Abstract

In this paper, an integrated optical fiber optoelectrode based on Fabry–Perot (F-P) cavity functionalized by ITO is first proposed to simultaneously realize the function of electrochemical working electrode and the function of fiber sensing. In the experimental prototype, the redox reaction of $K_3[Fe(CN)_6]$ system in electrochemical reaction was token as an example. Simultaneous monitoring of the electrochemical and optical responses of the optoelectrode at different scan rates is discussed. The results show that the electrochemical behavior of $K_3[Fe(CN)_6]$ and $K_4[Fe(CN)_6]$ on the surface of the F-P-ITO optoelectrode can be successfully monitored. As the electrochemical process proceeds, local refractive index changes around the optical fiber F-P-ITO optoelectrode dominated by diffusion control will induce an obvious shift in the interference spectrum. Significantly, this novel structure of integrated F-P optoelectrode functionalized by conductive ITO based on fiber interferometer has great potentials in the fields of electrochemistry systems and biomedical applications.

## 1. Introduction

Electrochemical analysis is an emerging and powerful analytical method in the fields such as chemistry, environment, biology and energy [1-8]. Electrochemical analysis methods can usually accurately analyze the chemical reactions occurring on the surface of the working electrode, especially the redox reactions. In recent years, to fully describe the details and complete information of the reaction process, electrochemical analysis processes based on real-time optical detection (such as real-time fluorescence, on-line Raman and other means) provide important process information for electrochemical reactions [9-11]. However, most of these systems are mechanical combinations of individual systems, the working electrode and light detection are separated structures. Then, it is difficult to realize structural integration and limits their practical application. Therefore, the integration of working electrode and high-sensitivity optical probe is an urgent problem to be solved.

On the other hand, with the rapid development of optical fiber technology, micro-nano structured optical fibers are widely used in the field of sensing [12-20]. Among them, the fiber F-P cavity probe with high quality interference spectrum has the characteristics of simple structure, small size, strong plasticity, and high sensitivity. It has attracted more and more attention [21-26]. Moreover, integrating functional materials of inorganic materials such as nanoparticles and organic molecules such as biological enzymes with optical fiber can realize the aim of optical fiber sensing in different fields [27-30]. Among them, Indium tin oxide (ITO) has excellent transparency and it is a narrow-bandgap semiconductor material, which gives it metal-like electrical conductivity. Compared with metals such as Au and Ag, the integration of ITO and fiber is more stable. (The metal film of Au and Ag integrated optical fiber is easy to fall off after the voltage is applied in the solution many times, which will affect the actual use effect.) Therefore, ITO is expected to realize the conductive function of optical fiber and be used to build photoelectric devices based on optical fiber.

In this paper, a novel optical fiber F-P optoelectrode for online real-time simultaneous electrochemical and optical monitoring is proposed for the first time. The optoelectrode was prepared by integrating a transparent conductive ITO film with an optical fiber F-P probe. The optoelectrode was used as the working electrode of the electrochemical analysis system to participate in the reaction, and at the same time, it was used as a sensing probe to detect the redox process in real-time online. In this experiment, $[Fe(CN)_6]^{3-}$ / $[Fe(CN)_6]^{4-}$ couple were taken as examples to monitor the redox reaction [31,32]. In the electrochemical process, local refractive index around the optoelectrode will change, which results in a shift in the interference spectrum. Through the integration of ITO with the fiber F-P probe, the novel fiber F-P optoelectrode can simultaneously monitor the information of the electrochemical and describes the changes of the environment around the optical fiber in real time. It is worth noting that the integrated ITO-fiber structure of this new optoelectrode realized the electrode function of the optical fiber F-P probe and will have wider range of applications and great potentials in photoelectric integrated system and electrochemical analysis such as energy electrochemistry systems and biomedical applications.

## 2. Experiment

### 2.1 Chemicals and Preparation process of optical fiber F-P-ITO cavity optoelectrode

KCl and ethanol were purchased from Zhiyuan Chemical Reagent Co. LTD. $K_3[Fe(CN)_6]$ and $K_4[Fe(CN)_6]$ were purchased from Aladdin reagent Company. The 3 dB coupler and single-mode

fiber used to make the interferometer were purchased from Yangtze Optical Fibre and Cable Joint Stock Limited Company. The optical fiber F-P cavity probe was fabricated by the fiber largely offset misalignment fusion splicing method [33]. Fig. 1 shows the manufacturing process of the F-P-ITO optoelectrode. Firstly, the 3 dB coupler and the single-mode fiber were fusion spliced with largely offset misalignment. The offset distance was 73 μm. Secondly, the single-mode fiber was cut to 150 μm (that is the length of the F-P cavity). Thirdly, the cut fiber and the single-mode fiber were fusion spliced with largely offset dislocation again. Finally, the fabricated optical fiber FPI was ultrasonically cleaned in water and ethanol and then it was sputtered twice by a commercially available RF magnetron sputtering system (JGP 450B) [34]. And, the optical fiber and the target are kept at an angle of 30° during sputtering to ensure that the continuous ITO film is integrated on the end face of the FPI. Here, the thickness of ITO film about 75 nm, which is measured by the 3D surface profiler (zygo), as shown in Fig. 2. When measuring film thickness, the sample surface is first pretreated and then coated with a gold film to increase reflection. As shown in Fig. 2(a), it is the 3D topography of the sample surface; Fig. 2(b) is the vertical section, and the difference between the maximum value and the minimum value is the ITO film thickness.

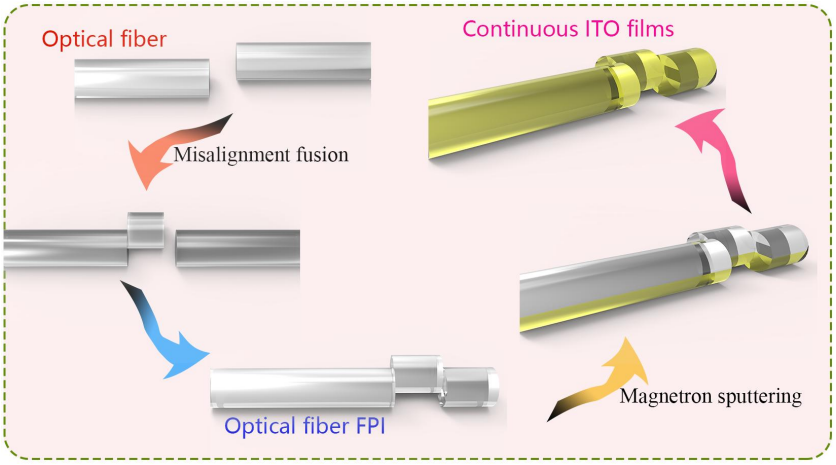


Fig. 1 Schematic diagram of the preparation of optical fiber F-P-ITO optoelectrode.

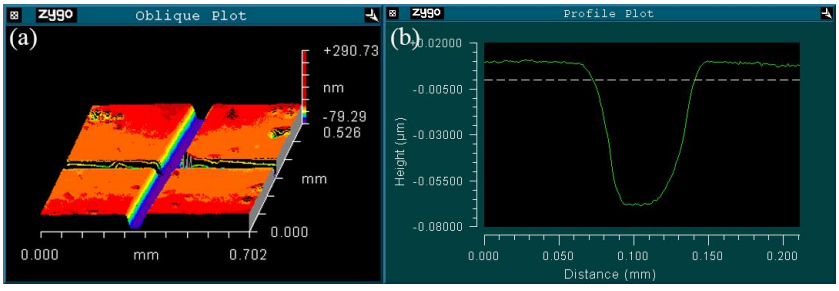


Fig. 2 Thickness of the ITO film measured on the upper surface of the fiber FPI. (a) The morphology of the film, (b) the thickness of the film.

### 2.2 Characterization of the optical fiber F-P-ITO optoelectrode

Fig. 3(a)-(b) shows the scanning electron microscope (SEM, Thermo Fisher Apreo C) images of different magnifications. It can see that the overall structure of the optical fiber F-P-ITO cavity optoelectrode and the smooth surface of the ITO film. Fig. 3(c)-(f) is an X-ray energy-dispersive spectroscopy (EDS, Oxford) of the optical fiber F-P-ITO cavity optoelectrode. In the figures, the distribution of Au, O, In and Sn elements on the surface of the optical fiber F-P-ITO optoelectrode

is shown, respectively. Au is sprayed over the entire sample surface as a conductive medium, so the Au element is distributed over the entire sample surface. Of which, O, In and Sn elements are distributed almost exclusively on the fiber F-P-ITO optoelectrode surface. The EDS elemental analysis spectrum is presented in Fig. 3(g). It can be seen from the figure that various elements on the surface of the fiber F-P-ITO optoelectrode are uniformly distributed. Fig. 3(h) presents the X-ray diffraction (XRD) spectrum of ITO film. The figure shows that the diffraction peaks of ITO correspond to PDF#39-1058. And the 30.272º, 35.164º, 50.976º and 59.938º correspond to (222), (400), (441) and (622) diffraction planes, respectively [35]. The optical fiber F-P cavity probe has been smoothly and uniformly modified by the ITO.

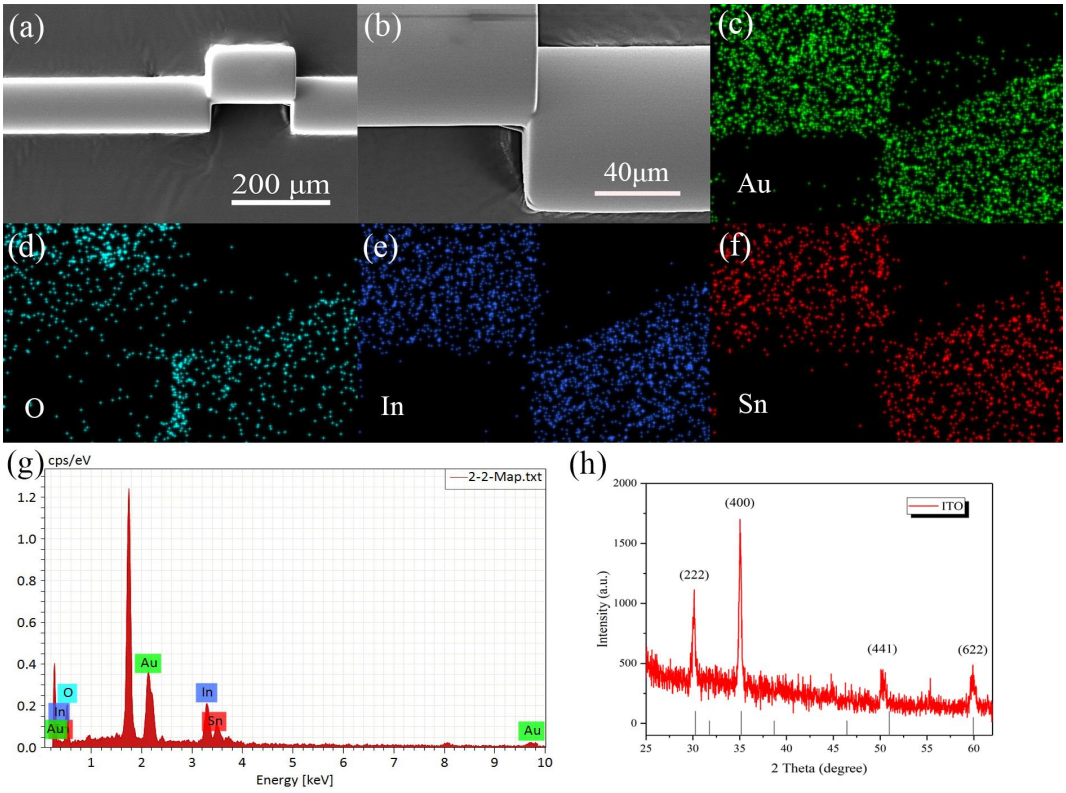


Fig. 3 Characterization diagram of fiber F-P-ITO optoelectrode. (a)-(b) The SEM images at different magnifications of the optical fiber F-P-ITO optoelectrode. (c)-(f) The EDS mapping images of Au, O, In, and Sn elements in the image (b). (g) EDS elemental analysis spectrum. (h) X-ray diffraction pattern of ITO film.

### 2.3 Construction of the optical fiber F-P-ITO cavity optoelectrode sensor

The experimental setup of the optical fiber F-P-ITO cavity optoelectrode sensor is shown in Fig. 4. An amplified spontaneous emission (ASE) light source was used as the experimental light source. An optical spectrum analyzer (OSA, AQ-6370) and monochromator were used as optical signal detectors. An electrochemical workstation (CHI 660E, Chenhua Instrument Shanghai Co., Ltd, China) was used for cyclic voltammetry and chronoamperometry measurements. In the electrochemical working system, the optical fiber F-P-ITO optoelectrode was used as the working electrode. Meanwhile, a piece of Pt foil and Ag/AgCl (saturated KCl) electrodes were used as counter and reference electrodes, respectively. The optoelectrode was connected with the light source and the detection device through a 3 dB coupler. The redox reaction between $[Fe(CN)_6]^{3-}$ and $[Fe(CN)_6]^{4-}$ is used as the reaction in the electrochemical reaction cell. KCl was used as the supporting electrolyte.

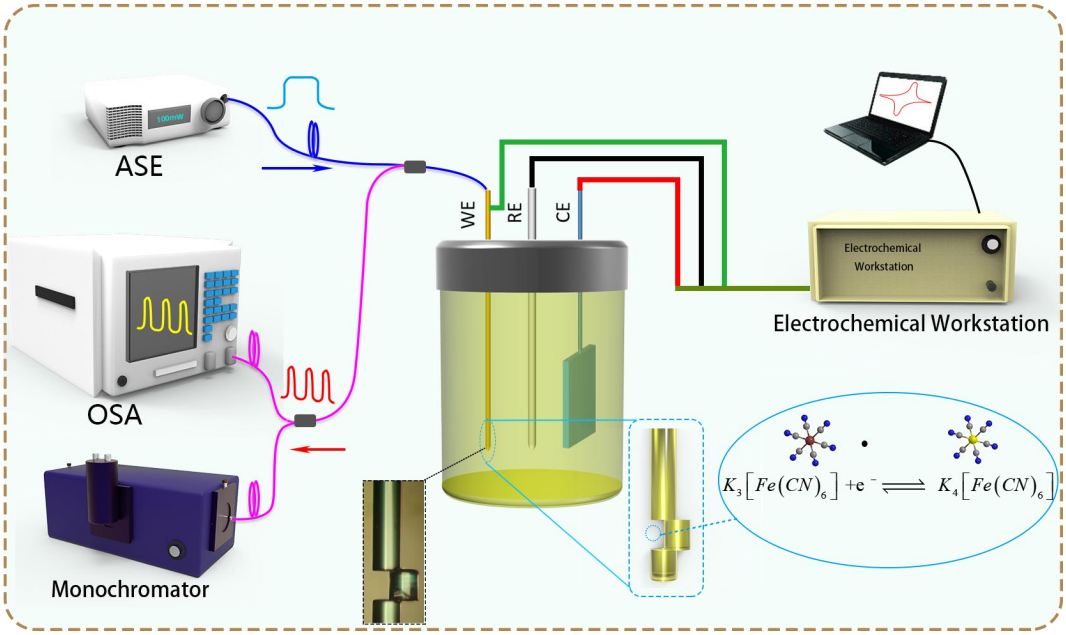


Fig. 4 Sensing device diagram of optical fiber F-P-ITO optoelectrode. Inset: microscope image of optical fiber F-P-ITO optoelectrode.

## 3. Results and discussion

### 3.1 RI sensitivity characteristics of the optoelectrode

First, the RI sensitivity of F-P-ITO optoelectrode was characterized and the results are shown in Fig. 5. Here, the fiber MZI was immersed in NaCl solutions with various RI at room temperature. The RI of the NaCl solution varies from 1.3320 to 1.3333, measured with an Abbe refractometer. The inset in Fig. 5 is the interference spectrum at different refractive indices. The inset clearly shows that the fiber F-P probe spectrum shifts significantly to the long-wavelength direction with RI increases. As shown in Fig. 5, the RI sensitivity of the fiber F-P-ITO optoelectrode was approximately 917 nm/refractive index unit (RIU) by fitting to the offset. The optoelectrode has great RI sensitivity, the phase shift has a favorable linear relationship with the refractive index change, and the correlation coefficient is higher than 0.99.

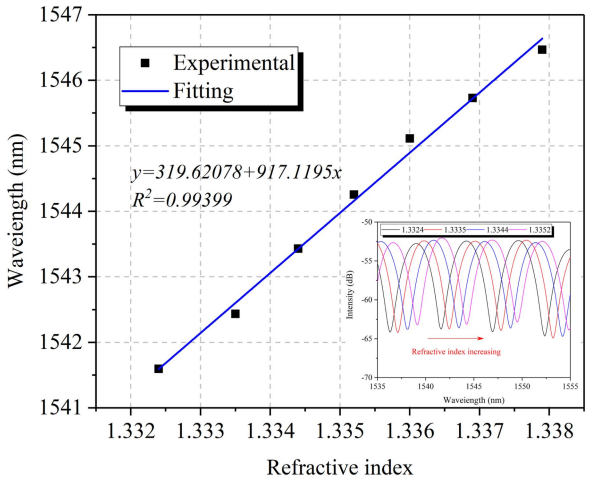


Fig. 5 Refractive index response of the optical fiber F-P-ITO optoelectrode. Inset: The interference spectrum moves when RI changes.

### 3.2 Spectral analysis at potentiostatic

In the experiment, $[Fe(CN)_6]^{3-}$ / $[Fe(CN)_6]^{4-}$ couple were taken as examples to monitor the redox reaction. Since the redox reaction between $[Fe(CN)_6]^{3-}$ / $[Fe(CN)_6]^{4-}$ pairs is one of the most classical reversible reactions in electrochemical reactions. Also, the reaction has an accurate redox potential and is often used as a standard reaction. Here, the optical fiber F-P-ITO optoelectrode was used as the working electrode and optical sensing probe for simultaneous electrochemical and optical measurements of electrochemical reactions. The electrochemical reaction solution contained 5 mM $K_3[Fe(CN)_6]$, 5 mM $K_4[Fe(CN)_6]$, and 0.1 M KCl. In this configuration, the potentials were controlled at 0.5 V to -0.5 V for an extended period to stabilize the potential and record the interference spectrum. The interference spectrum shift is shown in Fig. 6(a). As the potential changes from 0.5 V to -0.5 V, the interference spectrum shifts to the long-wave direction. Moreover, the interference spectrum changes significantly at negative potential. ITO is an n-type semiconductor, and most of its electrons act as carriers. According to the Drude Lorenz model, the real part of the semiconductor RI depends on the number of free carriers in the material [36,37]. By applying a negative potential, charges are transferred to the film, and the carrier concentration is higher near the ITO surface [38]. The real and imaginary parts of material RI are decreased and increased, respectively [39]. The inset in the figure is the interference spectrum in the 1535-1540 nm range. To observe the spectral shift more intuitively, we tracked the spectral intensity change at a fixed wavelength of λ = 1550 nm and summarize the results in Fig. 6(b). In the spectra, the light intensity at 1550 nm changes synchronously with the potential, which is consistent with the law of interference spectrum shift.

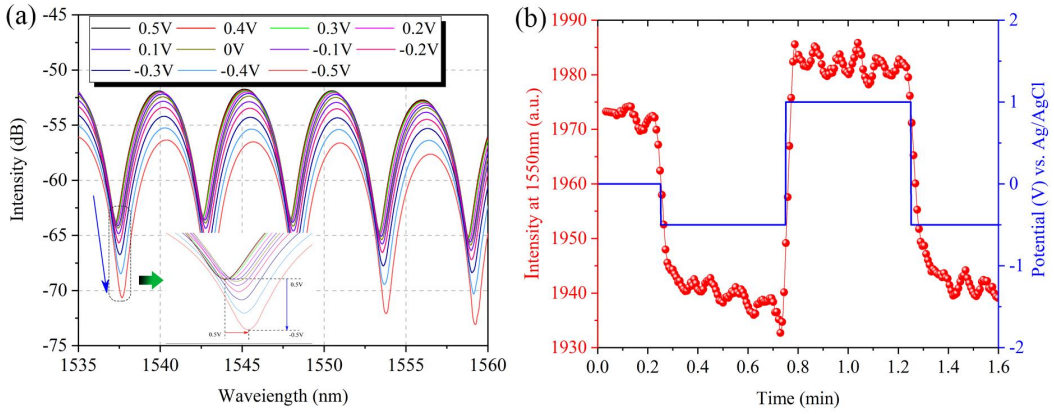


Fig. 6 The spectral analysis diagrams at different potentials. (a) The interference spectra at different potentials. Inset: The interference spectrum in the 1535-1540 nm range. (b) Spectral intensity changes at the wavelength of λ = 1550 nm.

### 3.3 Cyclic voltammetry electrochemical and optical analysis

The electrochemical behavior of the optical fiber F-P-ITO optoelectrode surface was investigated by cyclic voltammetry. $K_3[Fe(CN)_6]$ and $K_4[Fe(CN)_6]$ were used as representative redox indicators to evaluate the electrochemical performance of the sensor. The scan rates ranged from 10 to 500 mV/s and the cyclic voltammograms obtained are shown in Fig. 7(a). The cyclic voltammogram shows well-defined oxidation and reduction peaks, corresponding to the redox behavior of $[Fe(CN)_6]^{3-}$ and $[Fe(CN)_6]^{4-}$.Therefore, redox reactions on the surface of the optical fiber F-P-ITO optoelectrode was carried out by applying potentials ranging from -0.5 V to +1 V.

The results indicate that the spacing between the oxidation and reduction peaks in all experiments increased linearly with the scan rate. In addition, the positions of the oxidation peak and reduction peak at different scan rates are presented in Fig. 8. It can be seen from the figure that the increase of the scan rate leads to a positive shift of the oxidation peak potential and a negative shift of the reduction peak potential. This is mainly due to the diffusivity of each species in the redox reaction [40,41].

Fig. 7(b) shows the cyclic voltammetry curves of the reaction solution with or without $K_3[Fe(CN)_6]$ and $K_4[Fe(CN)_6]$. The scan rates were all 10 mV/s. The results show that the cyclic voltammetry curve of 0.1 M KCl solution had no obvious redox peak and approached a straight line. The inset of Fig. 7(b) is the cyclic voltammetry curve of the 0.1 M KCl solution after magnifying the ordinate.

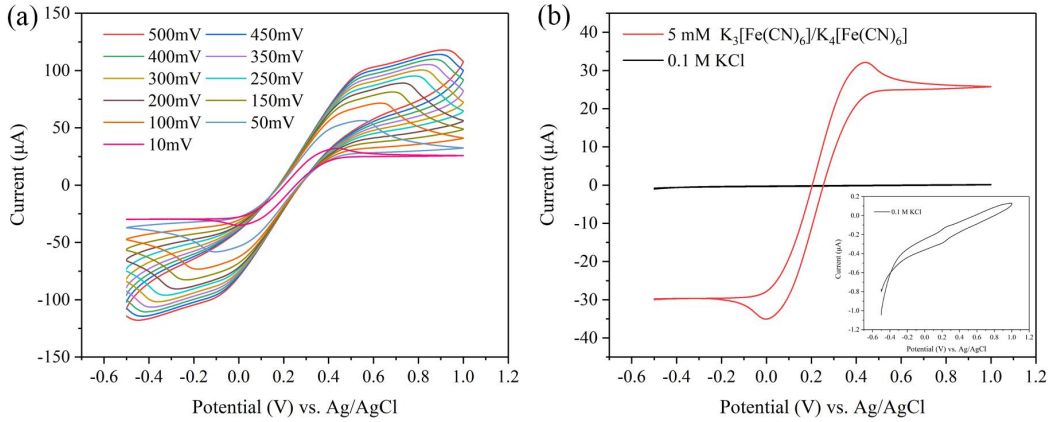


Fig. 7 Cyclic voltammograms of optical fiber F-P-ITO probe optoelectrodes. (a) Cyclic voltammograms with different scan speeds containing 5mM $K_3[Fe(CN)_6]$ and $K_4[Fe(CN)_6]$. (b) Comparison of scan rates of 10 mV/s. Inset: Cyclic voltammetry in 0.1 M KCl.

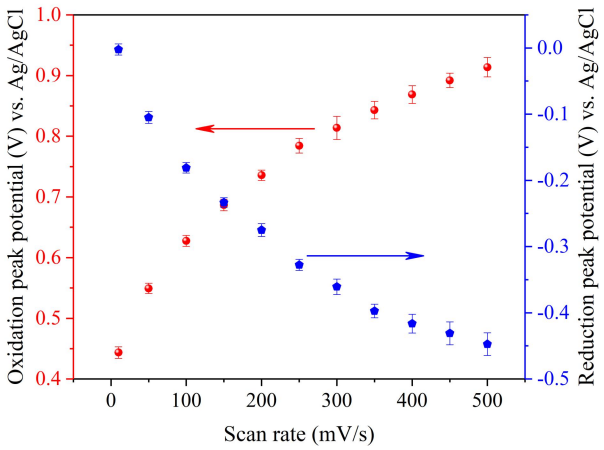


Fig. 8 Oxidation peak potentials and reduction peak potentials with different scan speeds.

During the cyclic voltammetry scan, the peak currents of the cathode and anode were measured simultaneously, as shown in Fig. 9. The results show that the cathodic ($i_{pc}$) and anodic ($i_{pa}$) peak currents increase with the scan rate. In addition, the peak current is proportional to the 0.5th power of the scan speed. Overall, the optical fiber F-P-ITO optoelectrode shows a current peak shift, which may correspond to the twice slower charge transfer process caused by certain charge blocking regions or surface energy barriers that require larger tunneling potentials [42].

After fitting the peak currents of the cathode and the anode, the correlation coefficients of the two currents both exceed 0.99. The fitting relations are $i_{pc}$ = *-29.40-130.55* $v^{1/2}$ and $i_{pa}$ = *26.59+133.71* $v^{1/2}$. The higher correlation coefficients indicate that the investigated electrochemical process is diffusion-controlled, as seen from the fit of the cathodic and anodic peak currents [43,44].

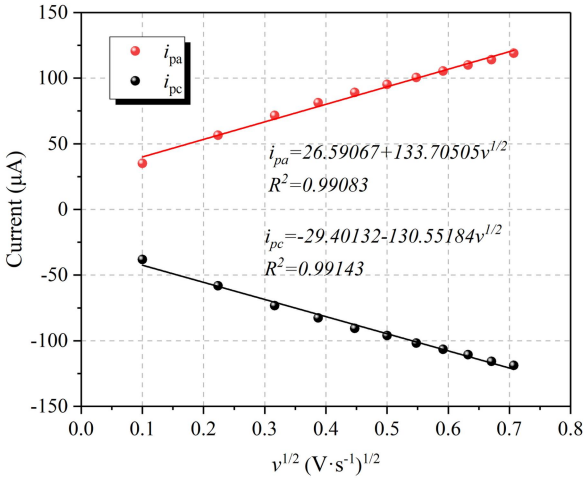


Fig. 9 Relations between *ipa* and *ipc* peak currents versus the square root of the scan rates.

The relationship between the redox peak current ratio and the scan rate is shown in Fig. 10(a). Only when the scanning speed is 10 mV/s, the ratio is slightly lower than 1, and the ratios are all around 1 at other rates. This number indicates that the reaction of $K_3[Fe(CN)_6]$ and $K_4[Fe(CN)_6]$ is a quasi-free reversible process. Fig. 10(b) shows the relationship between the logarithm of the redox peak current and the logarithm of the scan rate. Their fitting relationships are *log* $i_{pc}$ = *-2.17-0.31 log v* and *log* $i_{pa}$ = *2.18+0.33 log v*, respectively. The fitted relationships are 0.31 and 0.33, respectively, and $R^2$ is 0.999 and 0.999, respectively. These slopes are close to 0.5, which indicates that a diffusion-controlled process occurs near the fiber F-P-ITO optoelectrode [45]. Theoretically, a slope of 0.5 corresponds to the diffusion process, 1 to the adsorption process, and slopes between 0.5 and 1 belong to the mixed adsorption-diffusion control mechanism [46,47]. This result confirms that the electrochemical behavior of this electrochemical reaction on the fiber F-P-ITO probe optoelectrode is also diffusion-controlled.

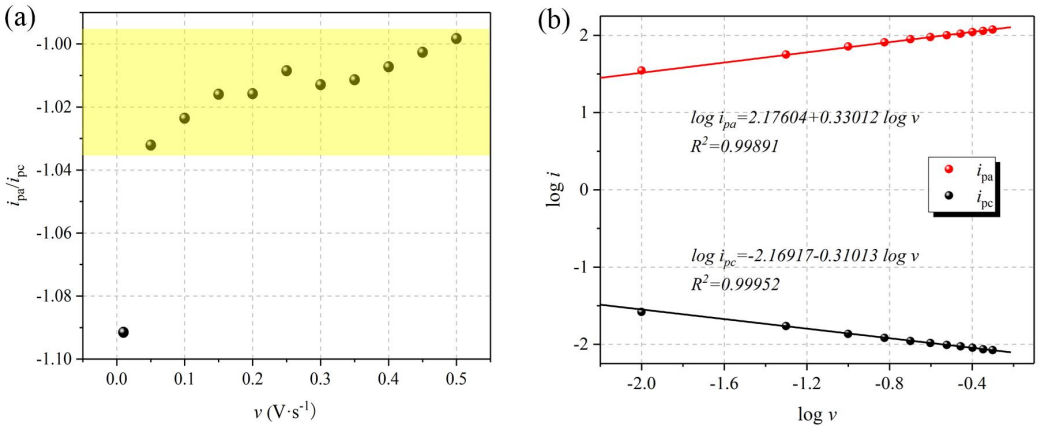


Fig. 10 (a) Peak current ratio versus different scan rate. (b) Relationship between the logarithm of the peak current and the logarithm of the scan rate.

Then, to more intuitively express the simultaneous electrochemical and optical sensing of this optoelectrode, the performance of the optoelectrode was further studied. The optical response of

the optical fiber F-P-ITO optoelectrode was investigated by cyclic voltammetry in KCl solution with 5 mM $K_3[Fe(CN)_6]$ and $K_4[Fe(CN)_6]$ added. Fig. 11 is a graph of the intensity of the interference spectrum at 1550 nm as a function of potential. The spectral intensities were recorded separately by the four different scan rates. Fig. 11(a)-(d) correspond to scan rates of 50, 100, 150, and 200 mV/s, respectively. The graph clearly shows great periodicity of the light intensity during cyclic voltammetry. The light intensity at a wavelength of 1550 nm increases with increasing potential. In addition, we repeated the test by varying the reactant concentration. Here, the concentrations of the reactants $K_3[Fe(CN)_6]$ and $K_4[Fe(CN)_6]$ are 7.5 mM and 2.5 mM, respectively. The optical response trends obtained are basically the same as those obtained when the reactant concentration is 5 mM. The optical response of the fiber F-P-ITO optoelectrode can show the existence of the redox reaction between $K_3[Fe(CN)_6]$ and $K_4[Fe(CN)_6]$ in real-time online. Therefore, in the proposed electrochemical system, the electrochemical process can be interconnected with the optical response of the probe. In other words, simultaneous online real-time electrochemical and optical measurements can be performed via the optical fiber F-P-ITO optoelectrode.

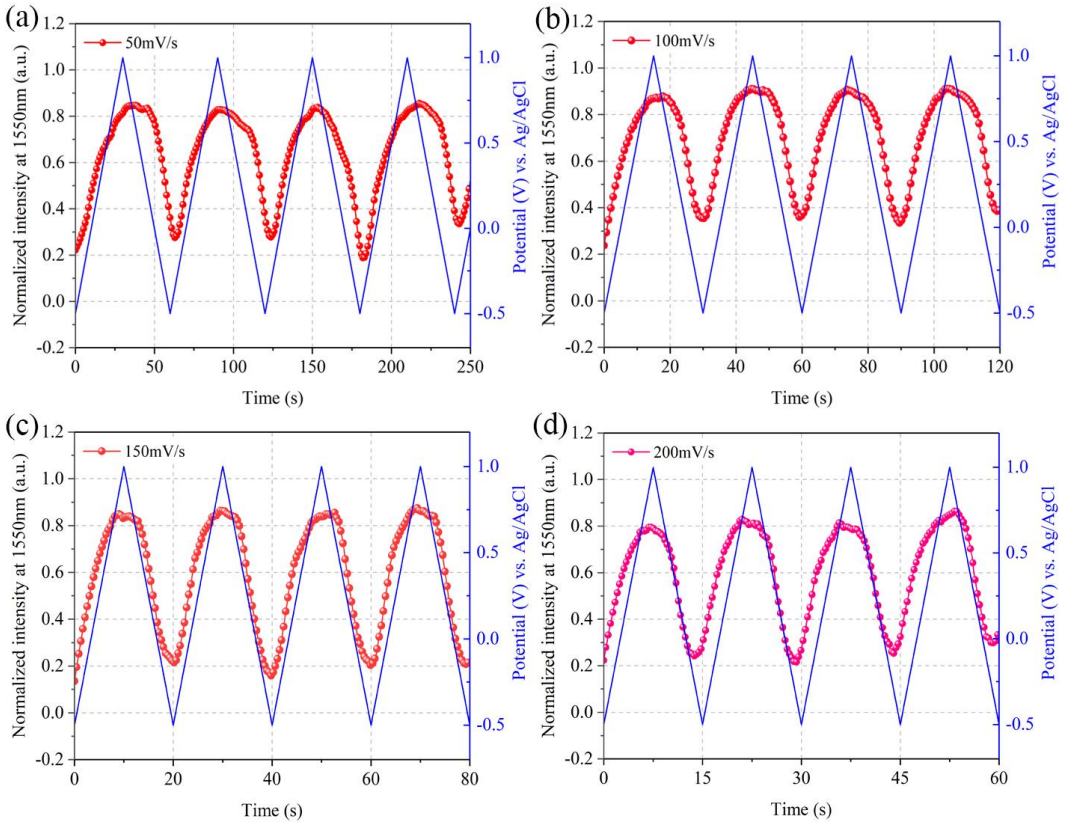


Fig. 11 Optical fiber F-P-ITO optoelectrode to potential cycling in 0.1 M KCl, 5 mM $K_3[Fe(CN)_6]$ and $K_4[Fe(CN)_6]$. Response at scan rate (a) 50, (b) 100, (c) 150, (d) 200 mV/s.

### 3.4 Chronoamperometry electrochemical analysis

The stability and repeatability of the optical fiber F-P-ITO optoelectrode were investigated by chronoamperometry. The real-time current intensity and light intensity at 1550 nm of the optoelectrode was recorded, as shown in Fig. 12. From the figure, it can see that when the current suddenly changes from positive to negative, the light intensity suddenly changes from high to low. The results can show that the optoelectrode exhibits obvious repeatability and stability after repeated cycling for many times. Fig. 13 shows the fall and rise times for one cycle. A fall time of

8 s and a rise time of 3 s are shown in the figure. The fiber F-P-ITO optoelectrode has a faster response speed.

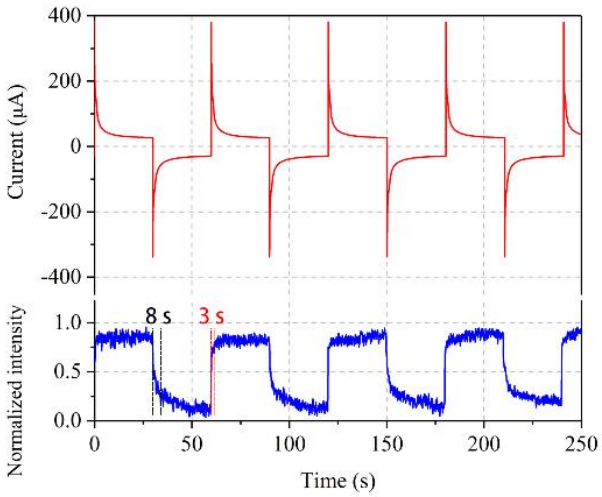


Fig. 12 Real-time light intensity of the optoelectrode at 1550 nm.

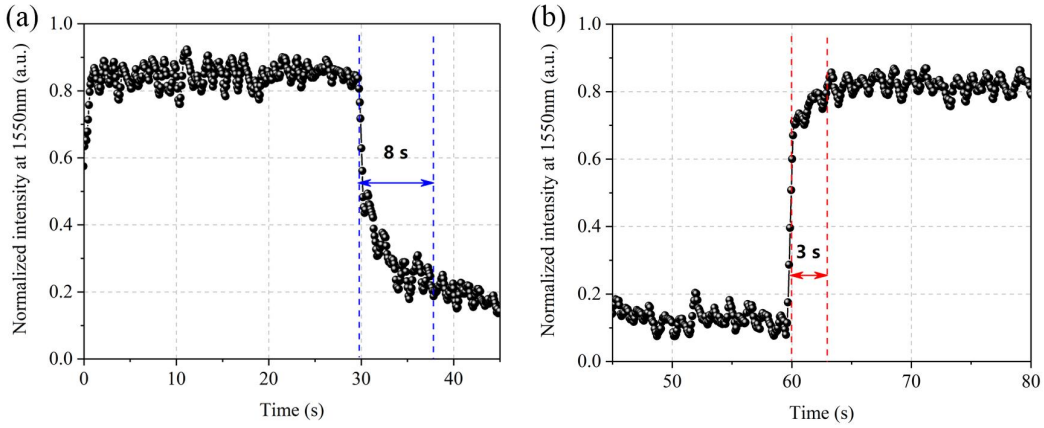


Fig. 13 Response time of the device at 1550 nm.

## 4. Conclusions

In this study, an optical fiber F-P-ITO optoelectrode was first proposed for simultaneous electrochemical and optical measurements. By integrating a conductive ITO film on the surface of the F-P probe, the optical fiber FP-ITO optoelectrode can be used as the working electrode of the electrochemical three-electrode system and the detection probe of the optical sensing system at the same time, which realized the simultaneous electrochemical and optical measurements. Specifically, when the electrochemical process, the effective refractive index near the F-P cavity changes, which in turn leads to a shift in the interference spectrum. The experimental results show that the electrochemical behavior measured at the optoelectrode is diffusion-controlled. And the intensity of the interference spectrum at 1550 nm changes periodically with the potential. Moreover, the optoelectrode shows repeatable and reversible optical properties. Optical fiber sensors usually have a lower detection limit, and at the same time have the characteristics of device miniaturization, rapid response, and detection sensitivity. On the other hand, electrochemical analysis methods can accurately and deeply analyze the biochemical reactivity of target media. This optical fiber F-P-ITO optoelectrode for simultaneous electrochemical and optical measurements has the characteristics of simple operation, convenient fabrication, remote

real-time monitoring, and easy integration with microstructure chips. Moreover, this photoelectrode can also be used as a basic platform to integrate other biochemical materials for label-free biochemical sensing. This compact optoelectrode combined with optical fiber interferometer and electrochemical measurements can efficiently collect more detection information than a single measurement method in the process of energy electrochemistry and biomedical such as Battery or biomedical monitoring.

## Notes

The authors declare no competing financial interest.


## Funding

National Natural Science Foundation of China (11574061, 62065001); Ministry of Science and Technology "High-end Foreign Expert Introduction Program"(G2022180002); Fundamental Research Funds for the Central Universities (3072022CF2506); Natural Science Foundation of Zhejiang Province of China (LGG20E040001).

## References


[1] Fujishima, A.; Honda, K. Electrochemical photolysis of water at a semiconductor electrode. *Nature* **1972**, *238*, 37-38.

[2] Sassa, F.; Biswas, G. C.; Suzuki, H. Microfabricated electrochemical sensing devices. *Lab Chip* **2020**, *20*, 1358-1389.

[3] Lahcen, A. A.; Rauf, S.; Beduk, T.; Durmus, C.; Aljedaibi, A.; Timur, S.; Alshareef, H. N.; Amine, A.; Wolfbeis, O. S.; Salama, K. N. Electrochemical sensors and biosensors using laser-derived graphene: A comprehensive review. *Biosens. Bioelectron.* **2020**, *168*, 112565.

[4] Zhang, X. R.; Sun, J.; Liu, J. S.; Xu, H. W.; Dong, B.; Sun, X. K.; Zhang, T. X.; Xu, S. H.; Xu, L.; Bai, X.; Zhang, S.; Mintova, S.; Lu, G. Y.; Song, H. W. Label-free electrochemical immunosensor based on conductive Ag contained EMT-style nano-zeolites and the application for α-fetoprotein detection, *Sensor. Actuat. B-Chem.* **2018**, *255*, 2919-2926.

[5] Berggren, M.; Malliaras, G. G. How conducting polymer electrodes operate. *Science* **2019**, *364*, 233-234.

[6] Lv, J. Q.; Xie, J. F.; Mohamed, A. G. A.; Zhang, X.; Wang, Y. B. Photoelectrochemical energy storage materials: design principles and functional devices towards direct solar to electrochemical energy storage. *Chem. Soc. Rev.* **2022**, *51*, 1511-1528.

[7] Tay, N. E. S.; Lehnherr, D.; Rovis, T. Photons or Electrons? A Critical Comparison of Electrochemistry and Photoredox Catalysis for Organic Synthesis. *Chem. Rev.* **2022**, *122*, 2487-2649.

[8] Mo, Y. M.; Lu, Z. H.; Rughoobur, G.; Patil, P.; Gershenfeld, N.; Akinwande, A. I.; Buchwald, S. L.; Jensen, K. F. Microfluidic electrochemistry for single-electron transfer redox-neutral reactions. *Science* **2020**, *368*, 1352-1357.

[9] Barnett, S. M.; Goldberg, K. I.; Mayer, J. M. A soluble copper-bipyridine water-oxidation electrocatalyst. *Nat. Chem.* **2012**, *4*, 498-502.

[10] Suseela, Y. V.; Narayanaswamy, N.; Pratihar, S.; Govindaraju, T. Far-red fluorescent probes for canonical and non-canonical nucleic acid structures: current progress and future implications. *Chem. Soc. Rev.* **2018**, *47*, 1098-1131.

[11] Wang, Y. H.; Zheng, S. S.; Yang, W. M.; Zhou, R. Y.; He, Q. F.; Radjenovic, P.; Dong, J. C.; Li, S. N.; Zheng, J. X.; Yang, Z. L.; Attard, G.; Pan, F.; Tian, Z. Q.; Li, J. F. In situ Raman spectroscopy reveals the structure and dissociation of interfacial water. *Nature* **2021**, *600*, 81-85.

[12] Gagliardi, G.; Salza, M.; Avino, S.; Ferraro, P.; De Natale, P. Probing the Ultimate Limit of Fiber-Optic Strain Sensing. *Science* **2010**, *330*, 1081-1084.

[13] Rein, M.; Favrod, V. D.; Hou, C.; Khudiyev, T.; Stolyarov, A.; Cox, J.; Chung, C. C.; Chhav, C.; Ellis, M.; Joannopoulos, J.; Fink, Y. Diode fibres for fabric-based optical communications. *Nature* **2018**, *560*, 214-218.

[14] Zhao, Y. J.; Zhou, A.; Guo, H. Y.; Zheng, Z.; Xu, Y. M.; Zhou, C. M.; Yuan, L. B. An Integrated Fiber Michelson Interferometer Based on Twin-Core and Side-Hole Fibers for Multiparameter Sensing. *J. Lightwave. Technol.* **2018**, *36*, 993-997.

[15] Taranta, A.; Fokoua, E. N.; Mousavi, S. A.; Hayes, J. R.; Bradley, T. D.; Jasion, G. T.; Poletti, F. Exceptional polarization purity in antiresonant hollow-core optical fibres. *Nat. Photonics* **2020**, *14*, 504-510.

[16] Consoli, A.; Caselli, N.; Lopez, C. Electrically driven random lasing from a modified Fabry-Perot

laser diode. *Nat. Photonics* **2022**, *16*, 219-225.

[17] Miele, E.; Dose, W. M.; Manyakin, I.; Frosz, M. H.; Ruff, Z.; De V., Michael F. L.; Grey, C. P.; Baumberg, J. J.; Euser, T. G. Hollow-core optical fibre sensors for operando Raman spectroscopy investigation of Li-ion battery liquid electrolytes. *Nat. Commun.* **2022**, *13*, 1651.

[18] Jousset, P.; Currenti, G.; Krawczyk, C. M. Fibre optic distributed acoustic sensing of volcanic events. *Nat. Commun.* **2022**, *13*, 1753.

[19] Murray, J. B.; Cerjan, A.; Redding, B. Distributed Brillouin fiber laser sensor. *Optica* **2022**, *9*, 80-87.

[20] Zaslawski, S.; Yang, Z. S.; Thevenaz, L. Distributed optomechanical fiber sensing based on serrodyne analysis. *Optica* **2022**, *8*, 388-395.

[21] Santos, J. S.; Raimundo, I. M.; Cordeiro, C. M. B.; Biazoli, C. R.; Gouveia, C. A. J.; Jorge, P. A. S. Characterisation of a Nafion film by optical fibre Fabry-Perot interferometry for humidity sensing. *Sensor. Actuat. B-Chem.* **2014**, *196*, 99-105.

[22] Li, M.; Liu, Y.; Gao, R. X.; Li, Y.; Zhao, X. L.; Qu, S. L. Ultracompact fiber sensor tip based on liquid polymer-filled Fabry-Perot cavity with high temperature sensitivity. *Sensor. Actuat. B-Chem.* **2016**, *233*, 496-501.

[23] Liu, Y.; Lang, C. P.; Wei, X. C.; Qu, S. L. Strain force sensor with ultra-high sensitivity based on fiber inline Fabry-Perot micro-cavity plugged by cantilever taper, *Opt. Express* **2017**, *25*, 7797-7806.

[24] Warren-Smith, S. C.; Andre, R. M.; Dellith, J.; Eschrich, T.; Becker, M.; Bartelt, H. Sensing with ultra-short Fabry-Perot cavities written into optical micro-fibers. *Sensor. Actuat. B-Chem.* **2017**, *244*, 1016-1021.

[25] Hou, M. D.; Liang, X. Y.; Zhang, T. T.; Qiu, C. Y.; Chen, J. D.; Liu, S. D.; Wang, W. J.; Fan, X. D. DNA Melting Analysis with Optofluidic Lasers Based on Fabry-Perot Microcavity. *ACS Sensors* **2018**, *3*, 1750-1755.

[26] Wang, X. D.; Wolfbeis, O. S. Fiber-Optic Chemical Sensors and Biosensors (2015-2019). *Anal. Chem.* **2020**, *92*, 397-430.

[27] Pathak, A.; Gupta, B. D. Fiber-Optic Plasmonic Sensor Utilizing CTAB-Functionalized ZnO Nanoparticle-Decorated Carbon Nanotubes on Silver Films for the Detection of Catechol in Wastewater. *ACS Appl. Nano Mater.* **2020**, *3*, 2582-2593.

[28] Bo, Y. T.; Guan, C. Y.; Chu, R; Cheng, T. L.; Xu, L.; Liu, L.; Yang, J.; Shi, J. H.; Wang, P. F.; Yang, J.; Yuan, L. B. Compact all-fiber thermo-optic modulator based on a Michelson interferometer coated with $NaNdF_4$ nanoparticles. *Opt. Express* **2021**, *29*, 6854-6862.

[29] Yang, X. H.; Yu, W. T.; Liu, Z. H.; Yang, J., Zhang, Y.; Kong, D.; Long, Q. L.; Yuan, T. T.; Cao, J. M.; Yuan, L. B.; Oh, K. Optofluidic twin-core hollowfiber interferometer for label-free sensing of the streptavidin-biotin binding. *Sensor. Actuat. B-Chem.* **2018**, *277*, 353-359.

[30] Samavati, A.; Samavati, Z.; Ismail, A. F.; Yahya, N.; Othman, M. H. D. Rahman, M. A. Multi aspect investigation of crude oil concentration detecting via optical fiber sensor coated with ZnO/Ag nano-heterostructure. *Measurement* **2021**, *167*, 108171.

[31] Rooney, M. B.; Coomber, D. C.; Bond, A. M. Achievement of near-reversible behavior for the $[Fe(CN)_6]^{3-/4-}$ redox couple using cyclic voltammetry at glassy carbon, gold, and platinum macrodisk electrodes in the absence of added supporting electrolyte, *Anal. Chem*. **2000**, 72, 3486-3491.

[32] Zhu, P.; Wang, Y.; Zhang, M. H.; Wu, Y. D.; Cai, W. F. Anions influence on the electrochemical performance of $Co_3X_4$ (X = O, Se) for supercapacitor: Experiments and theoretical calculations. *Appl. Surf. SCI.* **2022**, *574*, 151646.

[33] Deng, M.; Tang, C. P.; Zhu, T.; Rao, Y. J. Highly sensitive bend sensor based on Mach-Zehnder interferometer using photonic crystal fiber. *Opt. Commun.* **2011**, *284*, 2849-2853.

[34] Zamarreno, C. R.; Lopez, S.; Hernaez, M.; Del Villar, I.; Matias, I. R.; Arregui, F. J. Resonance-based refractometric response of cladding-removed optical fibers with sputtered indium tin oxide coatings. *Sensor. Actuat. B-Chem.* **2015**, *175*, 106-110.

[35] Wang, Y. H.; Liu, J.; Wu, X.; Yang, B. Adhesion enhancement of indium tin oxide (ITO) coated quartz optical fibers. *Appl. Surf. SCI.* **2014**, *308*, 341-346.

[36] Reed, G. T.; Png, C. E. J. Silicon optical modulators. *Mater. Today.* **2005**, 8, 40-50.

[37] Smietana, M.; Janaszek, B.; Lechowicz, K.; Sezemsky, P.; Koba, M.; Burnat, D.; Kieliszczyk, M.; Stranak, V.; Szczepanski, P. Electro-optically modulated lossy-mode resonance. *Nanophotonics* **2022**, *11*, 593-602.

[38] Ma, Z. Z.; Li, Z. R.; Liu, K.; Ye, C. R.; Sorger, V. J. Indium-Tin-Oxide for High-performance Electro-optic Modulation. *Nanophotonics* **2015**, *4*, 198-213.

[39] Han, X.; Mendes, S. B. Spectroelectrochemical properties of ultra-thin indium tin oxide films under electric potential modulation. *Thin Solid Films* **2016**, *603*, 230-237.

[40] Okazaki, T.; Shiokawa, E.; Orii, T.; Yamamoto, T.; Hata, N.; Taguchi, A.; Sugawara, K.; Kuramitz, H. Simultaneous Multiselective Spectroelectrochemical Fiber-Optic Sensor: Sensing with an Optically Transparent Electrode. *Anal. Chen.* **2018**, *90*, 2440-2445.

[41] Bard, A. J.; Faulkner, L. R. "Electrochemical Methods. Fundamentals and Applications" 2nd Ed. Wiley, New York. **2001**.

[42] Sezemsky, P.; Burnat, D.; Kratochvil, J.; Wulff, H.; Kruth, A.; Lechowicz, K.; Janik, M.; Bogdanowicz, R.; Cada, M.; Hubicka, Z.; Niedzialkowski, P.; Bialobrzeska, W.; Stranak, V.; Smietana, M. Tailoring properties of indium tin oxide thin films for their work in both electrochemical and optical label-free sensing systems. *Sensor. Actuat. B-Chem.* **2021**, *343*, 130173.

[43] Sherman, B. D.; Sheridan, M. V.; Dares, C. J.; Meyer, T. J. Two Electrode Collector-Generator Method for the Detection of Electrochemically or Photoelectrochemically Produced $O_2$. *Anal. Chen.* **2016**, *88*, 7076-7082.

[44] Govindaraju, G. V.; Wheeler, G. P.; Lee, D.; Choi, K. S. Methods for Electrochemical Synthesis and Photoelectrochemical Characterization for Photoelectrodes. *Chem. Mater.* **2017**, *29*, 355-370.

[45] Siuzdak, K.; Ficek, M.; Sobaszek, M.; Ryl, J.; Gnyba, M.; Niedzialkowski, P.; Malinowska, N.; Karczewski, J.; Bogdanowicz, R. Boron-Enhanced Growth of Micron-Scale Carbon-Based Nanowalls: A Route toward High Rates of Electrochemical Biosensing. *ACS Appl. Mater.* **2017**, *9*, 12982-12992.

[46] Batchelor-McAuley, C.; Goncalves, L. M.; Xiong, L. H. J.; Barros, A. A.; Compton, R. G. Controlling voltammetric responses by electrode modification; using adsorbed acetone to switch graphite surfaces between adsorptive and diffusive modes. *Chem. Commun.* **2010**, *46*, 9037-9039.

[47] Liu, T.; Hu, Y. T.; Chen, N.; He, Q. C.; Feng, C. P. High redox potential promotes oxidation of pyrite under neutral conditions: Implications for optimizing pyrite autotrophic denitrification. *J.*

*Hazard. Mater.* **2021**, *416*, 125844.